



Contents lists available at ScienceDirect

International Journal of Solids and Structures

journal homepage: www.elsevier.com/locate/ijsolstr

On the stress field ahead of a stationary crack tip during the transition from primary to secondary creep

John W. Sanders^{a,*}, Mohsen Dadfarnia^{b,c}, Huseyin Sehitoglu^d, James Stubbins^{c,e},
Petros Sofronis^{c,d}

^a Department of Mechanical Engineering, California State University, Fullerton, 800 North State College Boulevard, Fullerton, CA 92831, United States

^b Department of Mechanical Engineering, Seattle University, 901 12th Street, Seattle, WA 98122, United States

^c International Institute for Carbon-Neutral Energy Research (WPI-I2CNER), Kyushu University, 744 Motoooka, Nishi-ku, Fukuoka, Fukuoka 819-0395, Japan

^d Department of Mechanical Science and Engineering, University of Illinois at Urbana-Champaign, 1206 West Green Street, Urbana, IL 61801, United States

^e Department of Nuclear, Plasma, and Radiological Engineering, University of Illinois at Urbana-Champaign, 216 Talbot Laboratory, 104 South Wright Street, Urbana, IL 61801, United States

ARTICLE INFO

Article history:

Received 1 February 2019

Revised 19 January 2020

Accepted 28 February 2020

Available online 4 March 2020

Keywords:

Creep

Primary creep

Secondary creep

Power-law creep

Unified creep-plasticity

Kinematic hardening

Strain hardening

Recovery

Fracture

Cracking

Rupture

Compact tension specimen

Stress concentration

Stress relaxation

Asymptotics

Dimensional analysis

Superalloys

ABSTRACT

Despite the rich body of work on crack-tip asymptotics to date, the characterization of cracks in creeping solids remains an open problem. The purpose of this paper is to quantify the influence of primary creep on the near crack-tip stress field. We do this by simulating a classical compact tension test using a unified creep-plasticity model due to Robinson, Pugh, and Corum. This model accounts for the transition between primary and secondary creep organically through a kinematic hardening variable called the “internal flow stress” (which is related to the dislocation density of the material), and reduces to classical, power-law creep when the flow stress is negligible compared to the Cauchy stress. Stamm and Walz have shown that, in the limit of high stresses, the near crack-tip stress field predicted by the Robinson-Pugh-Corum model is well approximated by the so-called RR solution of Riedel and Rice, which was derived for power-law creeping solids. For low stresses, we find that the RR solution only applies when the primary creep response of the specimen is negligible. Indeed, the main contribution of this work is the identification of a dimensionless number Ξ , which characterizes the primary creep response of a compact tension specimen. When $\Xi \ll 1$, the specimen exhibits very little primary creep, and consequently, the RR solution is still accurate within a finite region ahead of the crack tip under both small-scale creep and extensive creep conditions. When $\Xi \gg 1$, the specimen exhibits significant primary creep, and consequently, the RR solution is *not* accurate under small-scale creep conditions (although remarkably there does appear to be a region in which the RR solution is still accurate under extensive creep conditions). Our results suggest that the relevant loading parameter is still the familiar stress intensity factor K_I under small-scale creep conditions, and the well-known C^* -integral under extensive creep conditions, regardless of the primary creep response of the specimen, in agreement with previous work.

© 2020 Elsevier Ltd. All rights reserved.

1. Introduction

Creep rupture is currently a major concern in many high-temperature energy conversion systems. To name one example, a leading design for next-generation nuclear reactors is the Very High Temperature Reactor (VHTR), in which temperatures are expected to reach anywhere from 650°C to 950°C (Chersola et al., 2015). Not only do such high temperatures have the potential to afford hitherto unprecedented thermal efficiency; they can also facilitate the thermo-chemical processing of hydrogen gas. However,

by the same token, such conditions are expected to place a severe burden on the Intermediate Heat Exchanger (IHX), and creep rupture is expected to be the primary failure mechanism. Despite the rich body of work on creep rupture to date, the characterization of the stress field ahead of cracks in creeping solids remains an open problem. In particular, very little work has been done on understanding how the near crack-tip fields behave—and what the relevant loading parameters are—during the transition from primary to secondary creep. The purpose of the present work is to gain further insight into the influence of primary creep on the near crack-tip fields.

Asymptotic crack-tip analyses have been carried out for a number of different material constitutive models. For isotropic,

* Corresponding author.

E-mail address: jwsanders@fullerton.edu (J.W. Sanders).

linearly elastic materials, Williams (1957) obtained the famous *singular elastic solution*, in which the asymptotic fields are controlled by the stress intensity factor K . Later, Hutchinson (1968) and Rice and Rosengren (1968) derived independently the celebrated *HRR solution*: the asymptotic fields in a material whose constitutive behavior is given by power-law strain-hardening plasticity. They found that the asymptotic fields are in general controlled by the J -integral (Eshelby, 1956; Rice, 1968). Under small-scale yielding conditions, it is well known that J is directly proportional to the stress intensity factor K , so that the asymptotic fields are still controlled by K under small-scale yielding conditions. These two solutions—the singular elastic solution (Williams, 1957) and the HRR solution (Hutchinson, 1968; Rice and Rosengren, 1968)—govern the stress field ahead of cracks in components operating near room temperature.

Riedel and Rice (1980) later revisited the asymptotic problem with power-law (secondary) creep in place of power-law hardening plasticity. By considering power-law creep, Riedel and Rice (1980) restricted attention to materials in which the primary creep response is negligible. Their solution, now known as the *RR solution*, is formally similar to the HRR solution, but with J replaced by a different path-independent integral $C(t)$, which is a rate-dependent analog to J . In the limit of very small times (and hence small-scale creep conditions), Riedel and Rice (1980) showed that $C(t)$ is directly proportional to J (with a time-dependent scaling factor), which is in turn proportional to K . Hence, under small-scale creep conditions, the fields are still controlled by K , even for power-law creep. In the limit of very large times, at which there is extensive creep of the entire specimen, $C(t)$ approaches a steady-state value C^* , and it is C^* that governs the magnitude of the asymptotic fields at large times.¹ The validity of the RR solution was verified numerically by Bassani and McClintock (1981). Riedel (1981) went on to perform similar analyses for a region of primary creep expanding within an elastic field, as well as a region of secondary creep expanding within a primary creep field, using power-law hardening models of primary and secondary creep. For small-scale primary creep, Riedel (1981)'s asymptotic solution, while different from the RR solution for small-scale power-law creep, is still controlled by the stress intensity factor K .

A limitation of the asymptotics literature cited above is the consideration of power-law hardening models of primary and secondary creep alone. Such models treat primary and secondary creep separately, and consequently fail to account for the transition from primary to secondary creep. This motivated the development of “unified creep-plasticity” models (Horstemeyer and Bammann, 2010). As the name suggests, such models capture (rate-dependent) plastic and primary/secondary creep deformation simultaneously by incorporating a local deviatoric tensor α_{ij} (referred to as the “internal flow stress,” or simply “flow stress” for short), which is mathematically analogous to the kinematic hardening variable of classical plasticity theory and helps to represent the material microstructure. The inelastic deformation is then formulated in terms of the effective stress $\bar{\Sigma}_{ij} = \sigma_{ij} - \alpha_{ij}$, which is simply the difference between the local Cauchy stress tensor σ_{ij} and the local flow stress tensor α_{ij} . At the very heart of these models is the particular dependence of the equivalent creep strain rate $\dot{\epsilon}^c$ on the Mises equivalent effective stress Σ_e :

$$\dot{\epsilon}^c = \dot{\epsilon}^c(\Sigma_e). \quad (1)$$

Bammann (1984), Enakoutsa et al. (2012), and Salehghaffari et al. (2012) have proposed a hyperbolic sine relation. Others have proposed an exponential relation (Horstemeyer and Bammann, 2010). Of particular interest in the present work,

¹ The interested reader will find a more detailed review of the RR solution in Appendix A.

Table 1

Limiting chemical composition of Alloy 230 HAYNES International. All values are percentage by weight.

Al	B	C	Co	Cr	Fe	La
0.3	0.015 (max)	0.1	5 (max)	22	3 (max)	0.02
Mn	Mo	Nb	Ni	Si	Ti	W
0.5	2	0.5 (max)	57 (balance)	0.4	0.1 (max)	14

however, is a model due to Robinson et al. (1976), who have proposed a power-law relation. The Robinson-Pugh-Corum model (or “RPC model,” for short) is distinctive in that it reduces to classical, power-law creep in the limit in which the flow stress α_{ij} is negligible compared to the Cauchy stress σ_{ij} . The flow stress itself evolves according to a differential equation of the form

$$\dot{\alpha}_{ij} = h\dot{\epsilon}_{ij}^c - r\alpha_{ij}, \quad (2)$$

where a superscribed dot denotes differentiation with respect to time t , $\dot{\epsilon}_{ij}^c$ is the creep strain rate tensor, and h and r are the hardening and recovery coefficients, respectively (not necessarily constants). As the names of the two coefficients h and r suggest, the first and second terms on the right-hand side of (2) represent strain hardening and recovery of the material, respectively. It is the competition between strain hardening and recovery that brings about the transition between transient and steady-state conditions, the latter of which corresponds to $\dot{\alpha}_{ij} = 0$. In a classical, uniaxial creep test, in which the applied stress is fixed, transient and steady-state conditions model primary and secondary creep, respectively. In a classical, uniaxial stress-strain test, in which the applied strain rate is fixed, steady-state corresponds to saturation of the axial stress at a constant value.

The crack-tip asymptotics of unified creep-plasticity models has received relatively little attention in the literature to date. One notable exception—and of particular relevance to the present paper—is the work of Stamm and Walz (1993) and Walz and Stamm (1993), who performed both analytical and numerical investigations of the crack tip fields associated with unified creep-plasticity models due to Robinson (1978) and Robinson and Swindeman (1982) (a generalization of the RPC model Robinson et al., 1976), as well as Chaboche (1989). Stamm and Walz (1993) and Walz and Stamm (1993) showed that, in the limit of high stresses, the stress field exhibits a singularity consistent with the RR solution of Riedel and Rice (1980). Ning and Hui (2012) further investigated the asymptotic stress field predicted by the Chaboche model (Chaboche, 1989), and they found that the region in which the RR solution is valid vanished at sufficiently large times. In the present work, we will identify more general conditions under which the RR solution (Riedel and Rice, 1980) approximates the near crack-tip stresses predicted by the RPC model (Robinson et al., 1976).

All simulations in the present work will be carried out for geometry representative of a compact tension specimen (which is the standard for assessing the versatility of fracture models), and for model parameters representative of real materials. The two materials of particular interest here are Alloy 230, which is used in gas turbine combustor liners and has recently been the subject of several experimental studies at high temperatures (Pataky et al., 2013; Tung et al., 2014; Maldini et al., 2010), as well as 2 1/4 Cr-1 Mo Steel, another high temperature alloy, which has been used in liquid metal cooled fast breeder reactor components (Robinson et al., 1976). The limiting chemical compositions of Alloy 230 HAYNES International and 2 1/4 Cr-1 Mo Steel are shown respectively in Tables 1 and 2. We will find that Alloy 230 and 2 1/4 Cr-1 Mo Steel are representative of materials that exhibit very little primary creep response and significant primary creep response, re-

Table 2

Approximate chemical composition of 2 1/4 Cr-1 Mo Steel Bro. All values are percentage by mass.

C	Cr	Fe	Mn	Mo	P	S	Si
0.05-0.15	2.0-2.5	95 (balance)	0.3-0.6	0.9-1.1	0.025	0.025	0.5

spectively. They are therefore good candidates for investigating the influence of primary creep on the near crack-tip stress field.

The remainder of this paper is organized as follows. In Section 2, we review the creep constitutive equations of Robinson et al. (1976) in detail, proposing two small modifications to the model to make its predictions more physically realistic. We also identify a useful time scale that characterizes the transition from primary to secondary creep in this model. In Section 3, we simulate compact tension tests of Alloy 230 at 800°C and 2 1/4 Cr-1 Mo Steel at 566°C using the RPC creep model (Robinson et al., 1976), and compare our numerical results to the RR solution of Riedel and Rice (1980). We find that there do, in fact, exist realistic conditions under which the RR solution does *not* give an accurate approximation to the near crack-tip fields, and we express those conditions in terms of a new dimensionless number Ξ , which characterizes the primary creep response of a compact tension specimen. In Section 4, we summarize our findings, and discuss the relevant loading parameters for materials undergoing a transition from primary to secondary creep.

2. The Robinson-Pugh-Corum (RPC) creep model

We review here the unified creep-plasticity model of Robinson et al. (1976), which captures both primary and secondary creep, with a smooth transition between the two. This model was originally formulated for small strains. Here, for the purposes of exploring the large-strain response, we will adopt finite strain formalism.

In the RPC model, the creep contribution to the rate-of-deformation tensor is given by

$$D_{ij}^c = \dot{\epsilon}^c N_{ij}, \quad (3)$$

where the equivalent creep strain rate $\dot{\epsilon}^c$ is

$$\dot{\epsilon}^c = A \Sigma_e^m, \quad (4)$$

and the tensor N_{ij} is

$$N_{ij} = \frac{3}{2} \frac{\Sigma'_{ij}}{\Sigma_e}. \quad (5)$$

In the above equations, the scalars A and m are temperature-dependent material parameters, the effective stress $\Sigma_{ij} = \sigma_{ij} - \alpha_{ij}$ is the difference between the local Cauchy stress tensor σ_{ij} and the local flow stress tensor α_{ij} , a subscript e denotes a Mises equivalent quantity such that, for any rank-two tensor T_{ij} ,

$$T_e = \sqrt{\frac{3}{2} T'_{ij} T'_{ij}}, \quad (6)$$

a prime denotes the deviatoric part of a tensor such that $T'_{ij} = T_{ij} - \frac{1}{3} T_{kk} \delta_{ij}$, where δ_{ij} is the rank-two identity tensor, and we are employing indicial notation (according to which subscript indices label tensor components and vary from 1 to 3) and the Einstein summation convention (according to which it is understood that repeated indices are summed over).

It should be noted that the mathematical form of (4) is reminiscent of classical, power-law creep. Indeed, the only difference in the mathematical formulations of the RPC model and the power-law model is the introduction of the flow stress α_{ij} . In going from power-law creep to RPC creep, one simply replaces the Cauchy stress σ_{ij} with the effective stress $\Sigma_{ij} = \sigma_{ij} - \alpha_{ij}$. Consequently, when the flow stress α_{ij} is negligible compared to the Cauchy

stress σ_{ij} , the effective stress is identical to the Cauchy stress, and RPC creep reduces to power-law creep. This is important, and we will return to this point later.

Physically, Robinson et al. (1976) interpret the flow stress as an internal state variable that represents the local material microstructure. In particular, they relate the equivalent flow stress α_e to the inherent resistance of the material to dislocation motion, setting

$$\alpha_e = B \sqrt{\rho}, \quad (7)$$

where ρ is the local dislocation density and the scalar B is a temperature-dependent material parameter. According to this interpretation of the flow stress, it is understood that the applied stress should exceed some critical value in order to cause dislocation motion (and thereby cause the material to creep). The effective stress Σ_{ij} is a measure of how much the applied stress exceeds said critical value. The time-dependence of the flow stress is governed by the following evolution equation:

$$\overset{\nabla}{\alpha}_{ij} = \frac{2C}{3\alpha_e} D_{ij}^c - D\alpha_e^2 \alpha_{ij}, \quad (8)$$

where the scalars C and D are temperature-dependent material parameters, and a superscribed triangle denotes the Jaumann rate-of-change, such that, for any rank-two tensor T_{ij} ,

$$\overset{\nabla}{T}_{ij} = \dot{T}_{ij} + T_{ik} W_{kj} - W_{ik} T_{kj}, \quad (9)$$

where W_{ij} is the skew-symmetric part of the velocity gradient.

2.1. Proposed modifications to the model

We note here that, even though the flow stress α_{ij} plays a similar role to the classical kinematic hardening variable, it does not make sense for it to be zero. Not only would this be physically unrealistic according to (7), since the dislocation density never vanishes, but it would also cause the hardening term in (8) to become singular. Robinson (1978), Robinson and Swindeman (1982) Stamm and Walz (1993), and Walz and Stamm (1993) set the flow stress to zero initially, and avoided the singularity in (8) by fixing the hardening and recovery coefficients until the dislocation density achieved a certain value. While there is nothing wrong with that approach from a mathematical standpoint, it does not seem consistent with the spirit of the model, in that it causes the physical interpretation of (7) to lose its meaning. In order to preserve the physical interpretation of (7), the flow stress must have a nonzero initial condition. Anticipating the compact tension test simulations presented in Section 3, we will take

$$\alpha(0) = \frac{1}{\sqrt{3}} B \sqrt{\rho_0} (\hat{\mathbf{e}}_x \otimes \hat{\mathbf{e}}_y + \hat{\mathbf{e}}_y \otimes \hat{\mathbf{e}}_x), \quad (10)$$

or, in matrix form,

$$[\alpha(0)] = \frac{1}{\sqrt{3}} B \sqrt{\rho_0} \begin{bmatrix} 0 & 1 & 0 \\ 1 & 0 & 0 \\ 0 & 0 & 0 \end{bmatrix}, \quad (11)$$

where ρ_0 is the initial dislocation density (for metals at high temperatures, ρ_0 is typically on the order of 10^{12} m/m³ (Hussein and El-Awady, 2016; Zhou et al., 2017)), and $\hat{\mathbf{e}}_x$ and $\hat{\mathbf{e}}_y$ point along the x - and y -axes shown in Fig. 5. We have omitted the out-of-plane components α_{xz} and α_{yz} in order to preclude out-of-plane deformation.

Now because we do not allow the flow stress to vanish, the model as it was originally formulated would predict physically unrealistic deformation in certain situations. For example, in the absence of external loading ($\sigma_{ij} = 0$), there should be no creep response in a material. However, even if the applied stress were zero, the effective stress $\Sigma_{ij} = -\alpha_{ij}$ would still be nonzero, and this would cause creep strain to accumulate according to (4). To remedy this, and in keeping with the spirit of the model, we propose modifying the flow rule (4) as follows:

$$\dot{\epsilon}^c = A \Sigma_e^m H(\sigma_e - \alpha_e), \quad (12)$$

where $H(\cdot)$ is the Heaviside step function. Eq. (12) states that creep strain accumulates only when $\sigma_e \geq \alpha_e$. Physically, the stress on a given lattice cell must exceed the microstructural resistance in order to induce creep at that point. Additionally, using (8), it can be shown that

$$\dot{\alpha}_e = C \alpha_e^{-2} D_{ij}^c \alpha_{ij} - D \alpha_e^3. \quad (13)$$

Under the modification described in (12), (13) predicts that, in the absence of external loading, in which case $D_{ij}^c = 0$, α_e (and therefore ρ) would tend to zero as time approaches infinity, another unrealistic result. To remedy this, we propose modifying the evolution Eq. (8) as follows:

$$\dot{\alpha}_{ij} = \frac{2C}{3\alpha_e} D_{ij}^c - D \alpha_e^2 \alpha_{ij} H(\alpha_e - B\sqrt{\rho_0}), \quad (14)$$

Eq. (14) prevents the dislocation density from falling below its original value. We will employ all of the above modifications in what follows. We note here that the present formulation of the model is intended specifically for monotonic loading configurations.

2.2. Calibration of the model parameters

The RPC model, as it has been formulated above, contains six temperature-dependent material parameters: A , B , C , D , m , and ρ_0 (although it should be noted that B and ρ_0 only appear in the combination $B\sqrt{\rho_0}$). As mentioned, ρ_0 can usually be estimated very reliably based on experimental measurements, and for metals at high temperatures it is typically on the order of 10^{12} m/m³ (Hussein and El-Awady, 2016; Zhou et al., 2017). The five remaining material parameters A , B , C , D , and m can be calibrated to a given alloy at a given temperature by fitting the model to experimental creep curves.

In the original work by Robinson et al. (1976), where the RPC model was first proposed, the model was calibrated to 2 1/4 Cr-1 Mo Steel at 566°C. A comparison between experimental uniaxial creep test data and the calibrated model predictions is shown in Figure 16 of Robinson et al. (1976), which we reproduce here as Fig. 1. The calibrated RPC model parameters reported in Robinson et al. (1976) are as follows: $A = 4.87 \times 10^{-40}$ Pa⁻⁴ · s⁻¹ (3.96×10^{-21} psi⁻⁴ · hr⁻¹), $B = 8.76$ Pa · m (0.05 psi · in), $C = 7.903 \times 10^{17}$ Pa² (1.6625×10^{10} psi²), $D = 2.382 \times 10^{-23}$ Pa⁻² · s⁻¹ (4.076×10^{-12} psi⁻² · hr⁻¹), and $m = 4$. Unfortunately, Robinson et al. (1976) did not report the initial dislocation density ρ_0 they used in their simulations, so this had to be estimated. From Eq. (16) (to be discussed shortly in Section 2.3), ρ_0 is related to the initial slope $\dot{\epsilon}_0^c$ of the creep curves by

$$\rho_0 = \left[\sigma - (\dot{\epsilon}_0^c/A)^{1/m} \right]^2 / B^2. \quad (15)$$

From the data shown in Fig. 1, we estimate that, for the curve labeled 69 MPa, $\dot{\epsilon}_0^c \approx 0.6 \times 10^{-2}/(200 \text{ hr})$. From this, we find the initial dislocation density to be $\rho_0 \approx 2.79 \times 10^{11}$ m/m³, which is a physically realistic value.

The RPC model has also been calibrated to Alloy 230 at 800°C according to a procedure developed by Sanders (2017), using experimental creep test data provided by Pataky et al. (2013) and

Table 3

Material parameters for Alloy 230 at 800°C and 2 1/4 Cr-1 Mo Steel at 566°C used in all simulations shown in the present work.

Parameter	Units	Alloy 230	2 1/4 Cr-1 Mo Steel
A	Pa ^{-m} · s ⁻¹	5.01×10^{-72}	4.87×10^{-40}
B	Pa · m	0.4162	8.76
C	Pa ²	8.67×10^{16}	7.9031×10^{17}
D	Pa ⁻² · s ⁻¹	1.00×10^{-16}	2.382×10^{-23}
m	-	8	4
ρ_0	m/m ³	1.00×10^{12}	2.79×10^{11}
E	GPa	190	140
ν	-	0.3	0.3

Maldini et al. (2010). A comparison between the model predictions and experimental creep test data is shown in Fig. 2, and a comparison between the model predictions and experimental stress-strain data is shown in Fig. 3. Because a perfect fit between the model predictions and all the experimental creep test data was not possible, priority was placed on matching the curve corresponding to the largest applied stress (i.e., 150 MPa) in Fig. 2. It is noteworthy that no information from the stress-strain curves was fed into the calibration procedure, and yet the model predictions in Fig. 3 follow the data reasonably well (at least in terms of order-of-magnitude). We interpret this as lending physical credibility to the RPC model.

The calibrated model parameters for both Alloy 230 at 800°C and 2 1/4 Cr-1 Mo Steel at 566°C are listed in Table 3. Also listed are Young's modulus E and Poisson's ratio ν , as these properties will be used in the simulations shown in Section 3. Young's modulus for Alloy 230 at 800°C was taken to be the average of that estimated from the data of Pataky et al. (2013) and that reported by HAYNES International HAYNES International. Young's modulus for 2 1/4 Cr-1 Mo at 566°C was estimated to be approximately 140 GPa based on the stress-strain data reported by Robinson et al. (1976). In both cases, a typical value of 0.3 was used for Poisson's ratio.

We note here that the creep curves for Alloy 230 from Maldini et al. (2010) in Fig. 2 exhibit essentially no primary creep, and consequently neither does the RPC model calibrated to Alloy 230 at 800°C. In contrast, the creep curves for 2 1/4 Cr-1 Mo Steel in Fig. 1 exhibit significant primary creep, and consequently so does the RPC model calibrated to 2 1/4 Cr-1 Mo Steel at 566°C. In short, Alloy 230 at 800°C and 2 1/4 Cr-1 Mo Steel at 566°C are representative of materials that exhibit negligible and significant primary creep response, respectively, and are therefore excellent candidates for investigating the effect of primary creep on the near crack-tip fields.

2.3. A time scale characterizing the transition from primary to secondary creep

The transition from primary to secondary creep is brought about through the flow stress α_{ij} by the competition between strain hardening and recovery processes. It will prove useful to identify a time scale that characterizes this transition. To that end, let us consider the reduced form of the constitutive equations in the case of uniaxial tension.

We take the z -axis to coincide with the loading direction. The only nonzero component of σ_{ij} is $\sigma_{zz} = \sigma$, where σ is the axially applied stress. Following Robinson et al. (1976), in this instance we will take the nonzero components of α_{ij} to be $\alpha_{zz} = \alpha$, $\alpha_{xx} = \alpha_{yy} = -\frac{1}{2}\alpha$. In such cases, (4) and (13) reduce to

$$\dot{\epsilon}^c = A(\sigma - B\sqrt{\rho})^m, \quad (16)$$

$$\dot{\rho} = \frac{2C}{B^2} \dot{\epsilon}^c - 2DB^2 \rho^2, \quad (17)$$

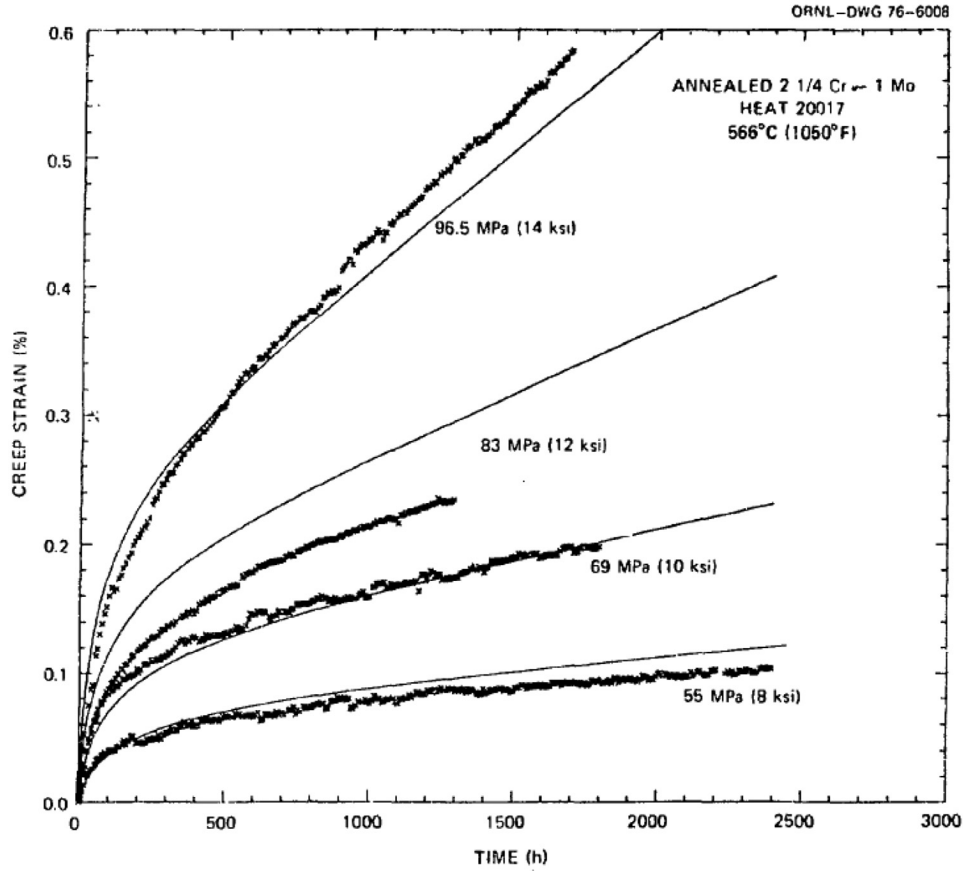


Fig. 1. Reproduction of Figure 16 from the original paper by Robinson et al. (1976), showing a comparison between model predictions and experimental creep test data for annealed 2 1/4 Cr-1 Mo Steel at 566°C. Used with permission.

where we have used (7) to express the equations in terms of ρ . In this form, the physical basis for the hardening and recovery terms becomes more clear. As noted by Robinson et al. (1976), (17) is consistent with a dislocation density evolution equation proposed by Lagneborg (1972), who reasoned as follows. In the absence of recovery, a small change in the dislocation density $d\rho$ gives rise to a small change in strain given by $d\varepsilon^c = b\ell d\rho$, where b is the magnitude of the Burgers vector and ℓ is the mean free path of dislocation motion. Lagneborg (1972) assumed that ℓ was approximately independent of ρ , so that, in the absence of recovery, $\dot{\rho} \propto \dot{\varepsilon}^c$. In the absence of hardening, when the dislocation line tension T provides the driving force for climb, the lattice size R_m evolves according to $\dot{R}_m = MTR_m^{-1}$, where M is the mobility of the climbing dislocation. Setting $R_m = \rho^{-1/2}$, Lagneborg (1972) found that $\dot{\rho} = -2MT\rho^2$, so that, in the absence of hardening, $\dot{\rho} \propto -\rho^2$. In this way, the evolution equation given by (14) is given a firm physical justification.

It is unclear whether the system of differential equations given by (16) and (17) has a general analytical solution. However, during a uniaxial stress-strain test, the total strain rate $\dot{\varepsilon}$ is held fixed, and if the exponent m is greater than unity, the elastic strain rate can be neglected in comparison to the creep strain rate, so that $\dot{\varepsilon}^c \approx \dot{\varepsilon} = \text{constant}$. In that case, the system given by (16) and (17) decouples, and an analytical solution is relatively straightforward.

Direct integration of (17) with constant $\dot{\varepsilon}^c$ yields

$$\frac{\rho}{\rho_\infty} = \tanh \left[2 \left(\frac{t}{\tau} \right) + \tanh^{-1} \left(\frac{\rho_0}{\rho_\infty} \right) \right], \quad (18)$$

where the steady-state dislocation density is given by

$$\rho_\infty = \frac{1}{B^2} \sqrt{\frac{C\dot{\varepsilon}^c}{D}}, \quad (19)$$

and we have defined a natural characteristic time τ by

$$\tau = \frac{1}{\sqrt{CD\dot{\varepsilon}^c}}. \quad (20)$$

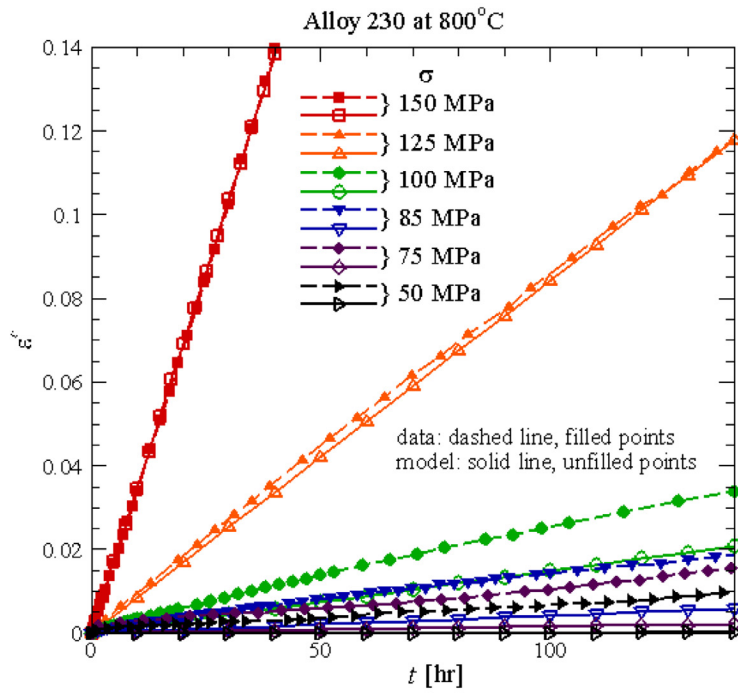
It is clear from (18) that τ characterizes the transition from primary to secondary creep. To get a quantitative idea of the role of τ , note that ρ_0/ρ_∞ is typically quite small. For example, for metals at high temperatures this ratio is on the order of 10^{-4} . In that case, when $t/\tau = 1$, $\rho/\rho_\infty \approx 0.964$. This means that, with $\rho_0/\rho_\infty = 1 \times 10^{-4}$, τ is the time required for ρ to reach 96.4% of its steady-state value.

Even when $\dot{\varepsilon}^c$ is not constant, we may still define a characteristic time inspired by (20). In particular, making use of (16), we can define a characteristic time as

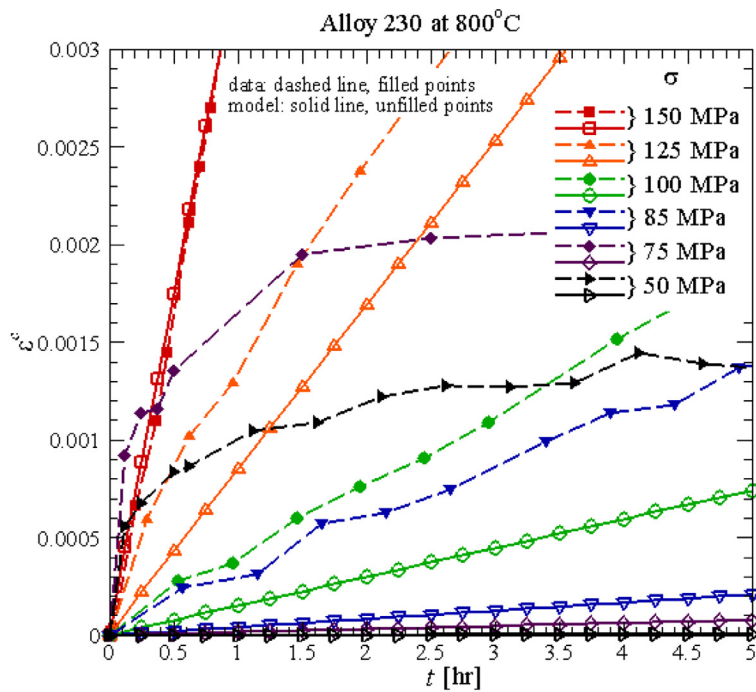
$$\tau = \frac{1}{\sqrt{ACD(\sigma^* - B\sqrt{\rho_0})^m}}, \quad (21)$$

where σ^* is some scalar measure of the applied stress (and it is understood that σ^* should be greater than $B\sqrt{\rho_0}$). Note that τ as defined by (21) depends on all five material parameters involved in the RPC model (A, B, C, D, m), the initial dislocation density ρ_0 (which, in a multiaxial simulation, dictates the initial value of the flow stress tensor), and a measure of the applied load. It is therefore representative of both the material and the loading conditions.

To check whether the characteristic time given by (21) does indeed provide a measure of the transition from primary to secondary creep, we will compute it for the creep curves shown in



(a)



(b)

Fig. 2. (a) Experimental creep test data for Alloy 230 at 800°C, along with corresponding numerical simulations of the RPC creep model with the calibrated parameters listed in Table 3. The data for the experiments at 50 MPa and 75 MPa come from Pataky et al. (2013), and the rest of the experimental data come from Maldini et al. (2010). (b) Close-up view of (a) at small times.

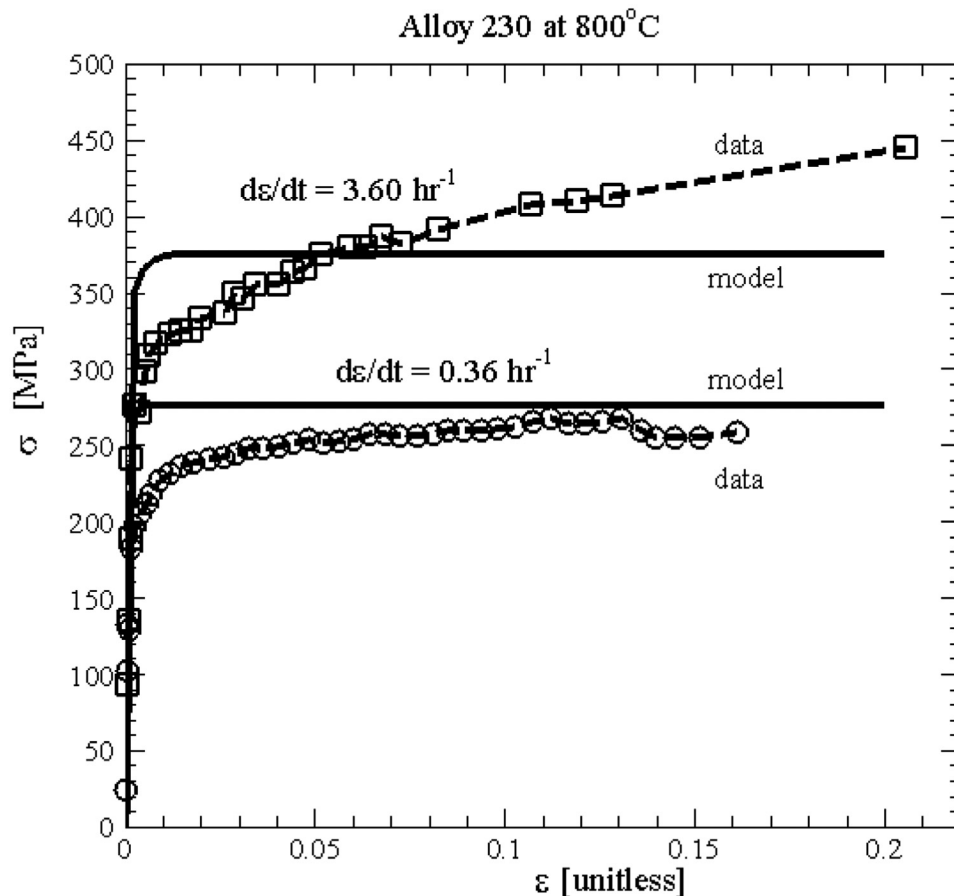


Fig. 3. Experimental stress-strain test data for Alloy 230 at 800°C, along with corresponding numerical simulations of the RPC creep model with the calibrated parameters listed in Table 3. The experimental data comes from Pataky et al. (2013).

Figs. 1 and 2 for 2 1/4 Cr-1 Mo Steel at 566°C and Alloy 230 at 800°C, respectively. For 2 1/4 Cr-1 Mo Steel at 566°C, we find that the transition times evaluated for the curves labeled 96.5 MPa, 83 MPa, 69 MPa, and 55 MPa in Fig. 1 come out to approximately 344 hr, 472 hr, 700 hr, and 1140 hr, respectively. For Alloy 230 at 800°C, we find that the transition times evaluated for the curves labeled 150 MPa, 125 MPa, 100 MPa, 85 MPa, 75 MPa, and 50 MPa in Fig. 2(a) come out to approximately 0.0842 hr, 0.175 hr, 0.429 hr, 0.823 hr, 1.36 hr, and 6.97 hr, respectively. Inspection of Figs. 1 and 2 confirms that these times reflect the transition from primary to secondary creep for the corresponding curves. Based on these results, τ as given by (21) appears to be a useful measure of the primary/secondary creep transition in the RPC creep constitutive model.

3. Compact tension test simulations

We now present simulations of a compact tension test using the general-purpose, finite element program ABAQUS. As noted in Section 2, the RPC creep model reduces to power-law creep when the flow stress is negligible compared to the Cauchy stress. Now it is well known that large stress concentrations develop near loaded crack tips, and these stress concentrations manifest as spatial singularities in the asymptotic fields. In contrast, the flow stress (which is proportional to the dislocation density) is always and everywhere finite. It seems reasonable, then, to expect that the flow stress should be negligible compared to the Cauchy stress sufficiently close to the crack tip. If that is the case, then the RR solution of Riedel and Rice (1980), which was derived for power-law

creep, should also be accurate even for RPC creep. In other words, it is tempting to assume that we can “get away with” the RR solution, even with the RPC creep model. However, we will see shortly that this is not always the case.

Fig. 4 illustrates the geometry of a standard, compact tension specimen ASTM E647-15e1. In Mode I tension, antiparallel forces F are applied at the two circular holes, as shown. The values of the reference dimensions considered in the present work are $a = 0.635$ cm and $w = 2.6416$ cm. Fig. 5(a) shows a simplified model of the compact tension specimen used in our simulations. The corresponding finite element mesh is shown in Fig. 5(b), and a close-up view of the notched crack tip is shown in Fig. 5(c), which also shows the coordinate system that will be used here. Standard, four-noded, plane strain, isoparametric elements were used in all simulations. The crack-tip notch has a radius of 12.7 μm , and the element size in the vicinity of the crack tip is 2.03 μm (about 16% the length of the notch radius). Due to the symmetry of the specimen and the applied loads, only the top half of the specimen is considered. The boundary conditions are also illustrated in Fig. 5(a). All nodes ahead of the crack tip along the symmetry plane are constrained in the vertical direction, and the bottom right node is completely fixed in order to prevent rigid body motion. A concentrated force of $F/10$ is applied at each of 10 nodes along the left-hand boundary. During all simulations, the applied force is increased from zero to its maximum value at a constant rate over a period of 1 s and held constant for the remainder of the simulation. This is done quickly so that the specimen does not have time to creep while the load is applied, and indeed $\tau \gg 1$ s in all cases. For a given value of F , the corresponding stress intensity factor K_I

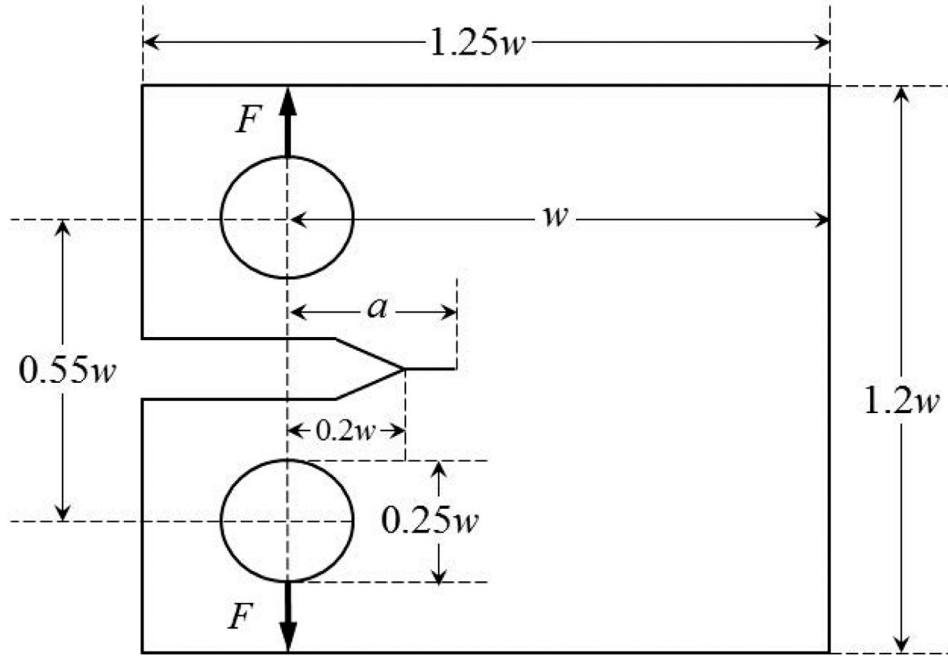


Fig. 4. Schematic diagram of a standard compact tension specimen ASTM E647-15e1, with relevant geometry labeled. Applied loads are illustrated for the case of Mode I tension.

for the compact tension specimen can be computed according to the following expression ASTM E647-15e1:

$$K_I = \frac{F}{b\sqrt{w}} g\left(\frac{a}{w}\right), \quad g(x) = \frac{2+x}{(1-x)^{3/2}} \times (0.886 + 4.64x - 13.32x^2 + 14.72x^3 - 5.6x^4). \quad (22)$$

In what follows, we consider two different applied loads, corresponding to $K_I = 15 \text{ MPa}\cdot\sqrt{\text{m}}$ ($F = 508.3 \text{ kN}$) and $K_I = 30 \text{ MPa}\cdot\sqrt{\text{m}}$ ($F = 1,017 \text{ kN}$). To facilitate discussion, we will refer to these as the “Small load” and “Large load,” respectively.

In the simulations presented here, the constitutive behavior of the material is modeled as a combination of isotropic, linear elasticity and incompressible creep (using either the RPC model or the classical, power-law model). In particular, the rate-of-deformation tensor D_{ij} is decomposed additively into an elastic component D_{ij}^e and a creep component D_{ij}^c , as follows:

$$D_{ij} = D_{ij}^e + D_{ij}^c, \quad (23)$$

where, according to Hooke's law,

$$D_{ij}^e = \frac{1}{E} \left[(1+\nu) \overset{\nabla}{\sigma}_{ij} - \nu \overset{\nabla}{\sigma}_{kk} \delta_{ij} \right], \quad (24)$$

E is Young's modulus, and is ν Poisson's ratio. For RPC creep, D_{ij}^c is given by (3) and the equations that follow, and this constitutive model has been implemented in ABAQUS® via a user-defined material subroutine (UMAT), the details of which can be found in Appendix E of Sanders (2017). For classical, power-law creep, the same equations hold in the absence of the flow stress, with creep exponent $m = n$ and creep modulus $A = \dot{\epsilon}_0 / \sigma_0^n$, where $\dot{\epsilon}_0 = 1 \times 10^{-6} \text{ s}^{-1}$ is the conventional reference strain rate and σ_0 is the reference stress for power-law creep.

We pause here to address a concern regarding the present formulation of the problem. The reflectional symmetry of the problem about the x -axis requires that $\alpha_{xy}(x, -y, t) = -\alpha_{xy}(x, y, t)$, and consequently that $\alpha_{xy}(x, 0, t) = 0$. A strict interpretation of the model leads to the conclusion that α_e (and thus the dislocation density ρ) must vanish along the symmetry axis at time $t = 0$ (note that the same conclusion does not apply for finite times $t > 0$, when the

flow stress α_{ij} develops nonzero components along the main diagonal). This issue does not arise in the present simulations, since we are only simulating the top half of the specimen ($y > 0$), where α_e is always and everywhere finite. Nevertheless, this issue is worth noting and needs to be resolved when the entire specimen is simulated.

3.1. A dimensionless number characterizing the primary creep response of a specimen

In Section 2.3, we defined a time scale τ , given by (21), that characterizes the transition from primary to secondary creep in the RPC model. For the purposes of computing τ for a compact tension test, we define the following stress-like measure of the applied load:

$$\sigma^* = K_I / \sqrt{a}, \quad (25)$$

which is simply the opening stress predicted by the singular elastic solution at a distance of $a/2\pi$ from the crack tip.

Riedel and Rice (1980) defined a second time scale relevant to the compact tension test, which characterizes the transition from small-scale creep to extensive creep of the entire specimen:

$$t_{RR} = \frac{(1-\nu^2)K_I^2}{(n+1)EC^*}, \quad (26)$$

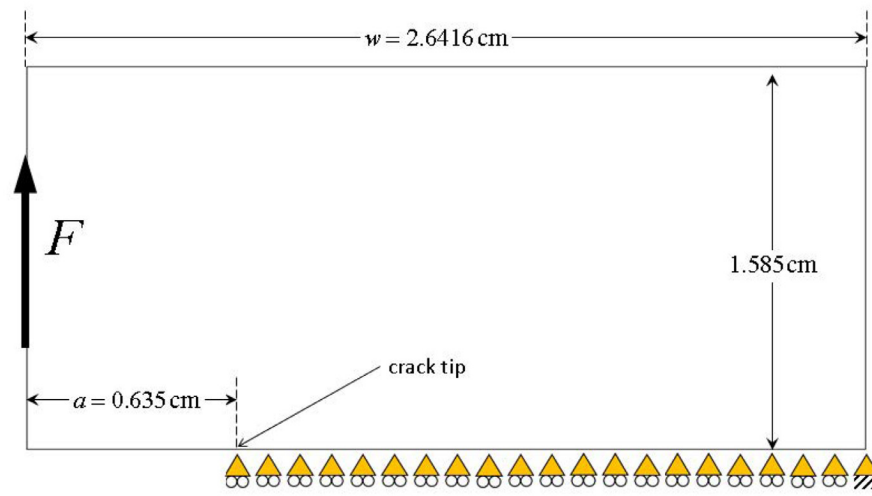
where n is the power-law creep exponent and C^* is the steady-state value of the C-integral, which can be determined from numerical analysis. For a Mode I test, it is found Kumar et al. (1981) that

$$C^* = \sigma_0 \dot{\epsilon}_0 c h_1(a/w, n) (F/F_0)^{n+1}, \quad (27)$$

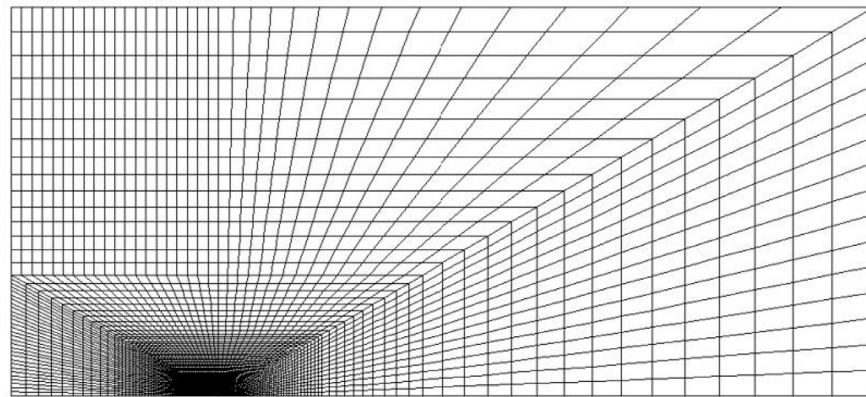
where σ_0 and $\dot{\epsilon}_0$ are the reference stress and strain rate, respectively, in the power-law creep model, $c = w - a$, numerical values for $h_1(a/w, n)$ are tabulated in Kumar et al. (1981), $F_0 = 1.455\eta c \sigma_0$, and

$$\eta = \left[4(a/c)^2 + 2(a/c) + 2 \right]^{1/2} - [2(a/c) + 1]. \quad (28)$$

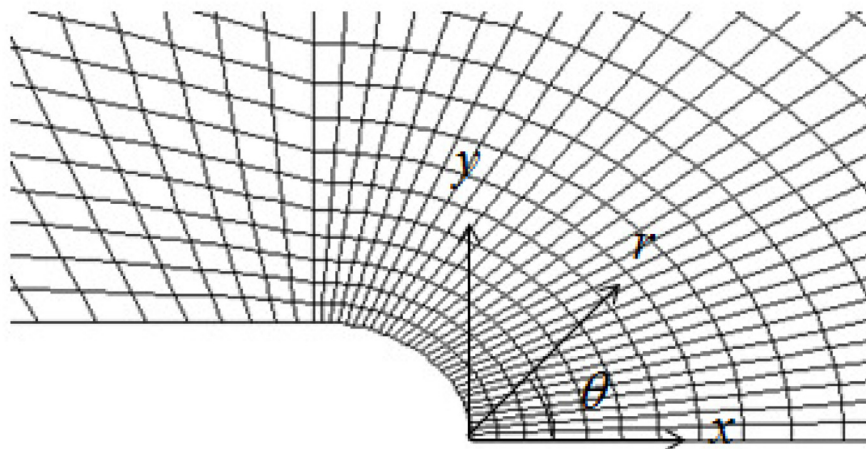
For more a slightly more detailed discussion of t_{RR} , see Appendix A.



(a)



(b)



(c)

Fig. 5. (a) Simplified model of the compact tension specimen, with applied load, boundary conditions, and relevant geometry labeled. Due to the symmetry of the problem, only the top half of the specimen is considered. (b) Corresponding mesh used for the finite element simulations in the present work. (c) Close-up view of the blunted crack tip.

We observe here that the following dimensionless number can be interpreted as a measure of the primary creep response exhibited by a given compact tension specimen:

$$\Xi \equiv \frac{\tau}{t_{RR}} = \frac{(n+1)EC^*\tau}{(1-\nu^2)K_I^2}, \quad (29)$$

where τ is given by (21). This Ξ is simply the ratio of two time scales: the time τ it takes the material to transition from primary to secondary creep, and the time t_{RR} it takes the specimen to transition from small-scale creep to extensive creep of the entire specimen. When $\Xi \ll 1$, it means that the transition to secondary creep occurs long before the transition to large-scale creep, that is, that the time spent in the primary creep regime is negligible, and hence that the specimen exhibits negligible primary creep. When $\Xi \gg 1$, it means that the transition to secondary creep occurs long after the transition to large-scale creep, that is, that the time spent in the primary creep regime is significant, and hence that the specimen exhibits significant primary creep. This number Ξ will prove very useful in making sense of our simulation results, which we now present.

In what follows, all simulation results will be suitably normalized. We note that there are two candidate time scales: τ and t_{RR} , either one of which could be used to normalize time. We have chosen to normalize all times by τ , so that the dimensionless time t/τ gives an indication of whether the specimen is undergoing mainly primary ($t/\tau < 1$) or secondary ($t/\tau > 1$) creep. Similarly, there are two candidate reference stresses: σ^* , as given by (25), as well as the following reference stress, which is defined in analogy to the reference stress of power-law creep:

$$\sigma_0 = (\dot{\epsilon}_0/A)^{1/m}, \quad (30)$$

where $\dot{\epsilon}_0 = 1 \times 10^{-6} \text{ s}^{-1}$. We note that σ^* varies depending on the applied load, whereas σ_0 remains constant for a given material at a given temperature. Therefore, in order to facilitate comparison between the results for the two loading levels, we have chosen to normalize all stresses by σ_0 .

3.2. Alloy 230 at 800°C

We begin with results for Alloy 230 at 800°C. The calibrated material parameters listed in Table 3 for Alloy 230 at 800°C yield the following reference quantities. The reference stress is $\sigma_0 = 145.4 \text{ MPa}$. For the Small and Large loads, τ comes out to about 0.0340 hr and 0.00211 hr, respectively, and likewise, t_{RR} comes out to about 19.3 hr and 0.151 hr, respectively (here we have set $n = m$). The dimensionless number $\Xi = \tau/t_{RR}$ is therefore about 0.00175 and 0.0140, respectively. These values, being much less than one, are consistent with the observation that Alloy 230 at 800°C exhibits very little primary creep.

Fig. 6 shows the opening stress distributions (σ_{yy}/σ_0 versus r/a) directly ahead of the crack tip (i.e., at $\theta = 0$) at various times for the two loading levels, using the RPC creep constitutive model calibrated to Alloy 230 at 800°C. Superimposed on each figure are the singular elastic solution

$$\sigma_{yy}|_{\theta=0} = K_I/\sqrt{2\pi r}, \quad (31)$$

and the corresponding RR solutions at the same times. By the “corresponding RR solutions,” we mean the RR solutions with the same reference stress σ_0 and creep exponent $n = m = 8$ (refer to Appendix A). Here we have estimated $\bar{\sigma}_{yy}(0, 8) \approx 2.4$ and $I_8 \approx 4.7$ from Figures 5.12 and 5.14 of Kanninen (1985).

It can be seen from Fig. 6(a) that, for the Small load at the smallest time shown ($t/\tau = 5.03 \times 10^{-2}$), there is a region ($r/a < 7 \times 10^{-3}$) in which the stress increases with distance from the crack tip; this is due to crack-tip blunting. At larger distances,

the stress starts to decrease, and the singular elastic solution becomes a fairly accurate approximation to the numerically simulated field. Then, as time increases, a region starts to form in which the RR solution is an accurate approximation to the numerically simulated field. This is apparent at $t/\tau = 4.72 \times 10^0$ for distances $7 \times 10^{-3} < r/a < 5 \times 10^{-2}$, at $t/\tau = 5.50 \times 10^1$ for distances $7 \times 10^{-3} < r/a < 1 \times 10^{-1}$, and at $t/\tau = 8.20 \times 10^2$ for distances $7 \times 10^{-3} < r/a < 2 \times 10^{-1}$. We note that four of the five times shown ($t/\tau \leq 5.50 \times 10^1$) are less than $t_{RR}/\tau = 570$, which means that small-scale creep conditions prevail for these four simulations. The fifth time shown ($t/\tau = 8.20 \times 10^2$) is greater than $t_{RR}/\tau = 570$, which means that at that time the specimen is exhibiting extensive creep (and the RR solution curve for $t/\tau = 8.20 \times 10^2$ corresponds to the RR solution for extensive creep). We have therefore shown that, for the Small load, there is a region in which the RR solution is valid under both small-scale creep and extensive creep conditions.

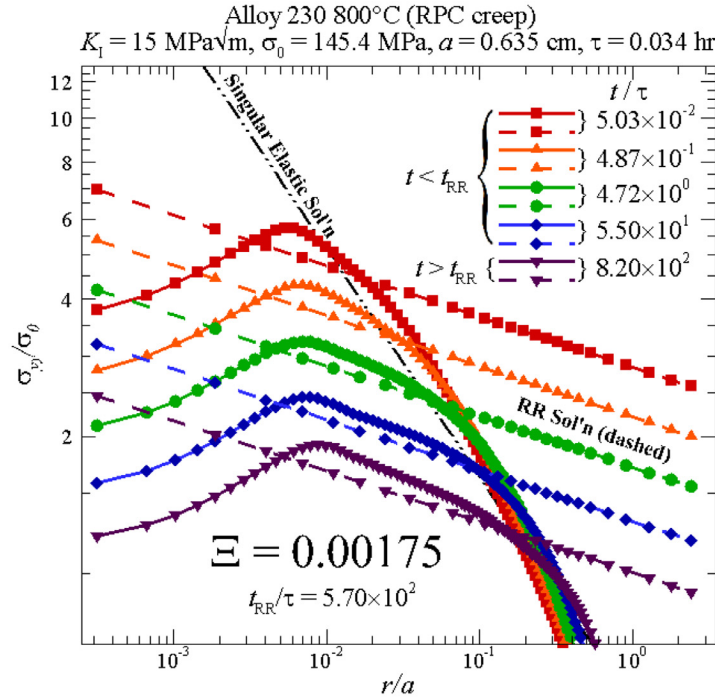
Fig. 6 (b) shows similar plots to Fig. 6(a) for the Large load. The qualitative behavior is much the same as that in Fig. 6(a). There still develops a region in which the RR solution is accurate under both small-scale creep and extensive creep conditions. However, the offset between the numerically simulated curves and the RR solution curves is slightly larger in Fig. 6(b) than it is in Fig. 6(a). That is, the numerical solution for RPC creep deviates from the RR solution to a greater degree for the Large load than it does for the Small load. It is interesting to note that, for both applied loads, there is a region in which the RR solution is approximately valid, even though we are using the RPC creep model instead of power-law creep, for which the RR solution was originally derived.

At this point, it is useful to compare Fig. 6 to what it would have looked like using power-law creep (with the same creep modulus $A = \dot{\epsilon}_0/\sigma_0^n$ and creep exponent $n = m$). The results for power-law creep are shown in Fig. 7. If the flow stress were indeed negligible compared to the Cauchy stress near the crack tip, we would expect Figs. 6 and 7 to be identical (or nearly so). In fact, that is precisely what we observe. The only major difference between the two figures is that the offset between the numerically simulated curves and the corresponding RR curves is slightly smaller in Fig. 7 than it is in Fig. 6. In other words, not unsurprisingly, the RR solution is more accurate for power-law creep than it is for RPC creep, although the difference is extremely small.

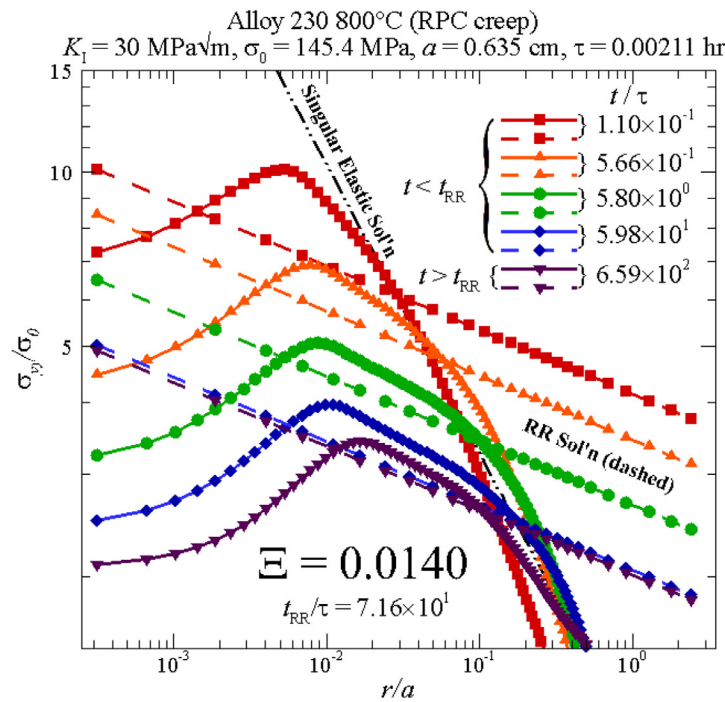
Before we move on, it is of interest to verify whether the flow stress is indeed negligible compared to the Cauchy stress for the numerical simulations shown in Fig. 6. Fig. 8 shows the distributions of the ratio α_e/σ_e directly ahead of the crack tip at various times for the two applied loads. It can be seen from Fig. 8 that α_e is rather small compared to σ_e at all of the times simulated for both applied loads. In particular, the ratio α_e/σ_e peaks at about 10% for the Small load and 14% for the Large load at the first times shown. The ratio quickly decreases to quantities on the order of 1% at subsequent times. This appears to confirm that the flow stress is indeed negligible compared to the Cauchy stress for these simulations, and that is why there is little difference between the RPC and power-law creep models. However, we emphasize that the model calibrated to Alloy 230 at 800°C exhibits essentially no primary creep. In retrospect, then, these results are not very surprising. To see the effect of primary creep, we turn to 2 1/4 Cr-1 Mo Steel at 566°C.

3.3. 2 1/4 Cr-1 Mo Steel at 566°C

The material parameters listed in Table 3 for 2 1/4 Cr-1 Mo Steel at 566°C yield the following reference quantities. The reference stress is $\sigma_0 = 212.9 \text{ MPa}$. For the Small and Large loads, τ comes out to 86.1 hr and 21.0 hr, respectively, and likewise, t_{RR} comes out to 5.68 hr and 0.710 hr, respectively (again, we have



(a)



(b)

Fig. 6. Numerically simulated opening stress distributions (solid curves) directly ahead of the crack tip (i.e., along the line $\theta = 0$) at various times with RPC creep for (a) the Small load and (b) the Large load. Superimposed are the singular elastic solution (dashed black line) and the corresponding RR solutions (dashed colored lines) at the same times. The material parameters represent Alloy 230 at 800°C. (For interpretation of the references to color in this figure legend, the reader is referred to the web version of this article.)

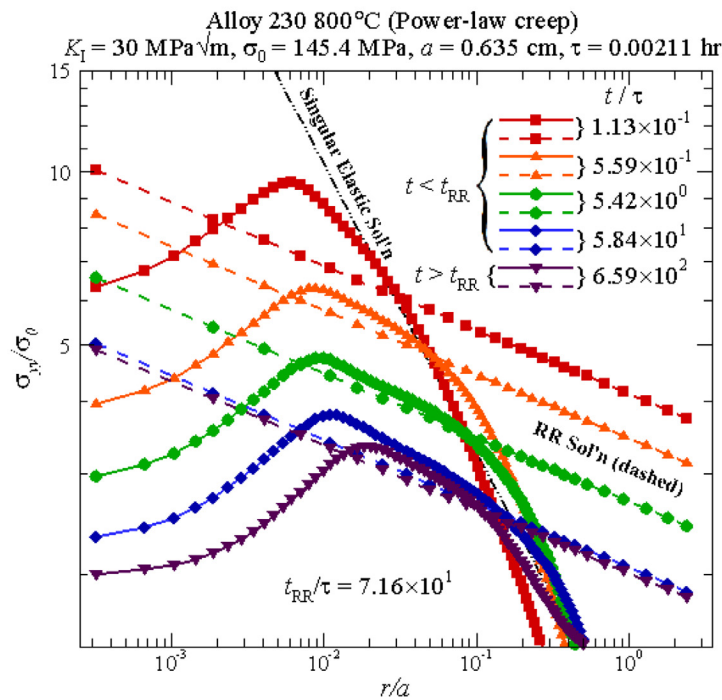
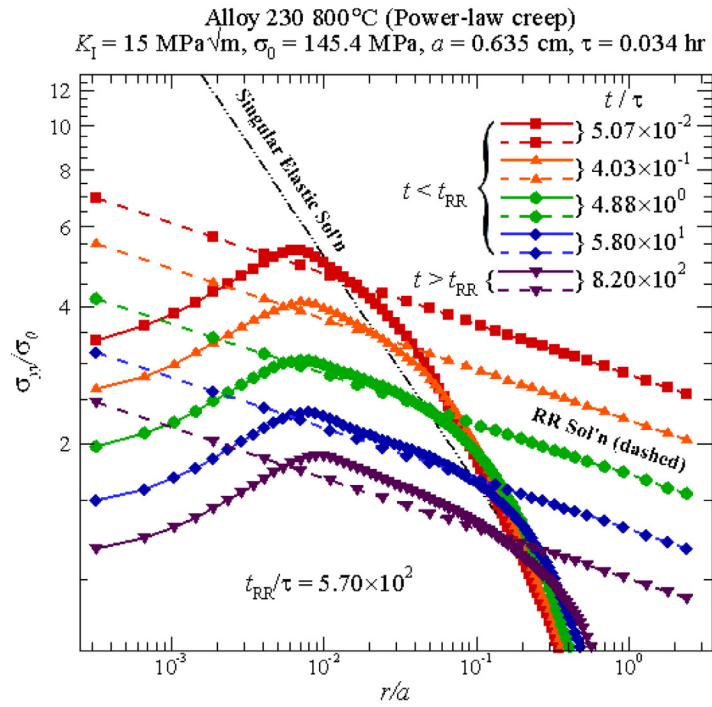
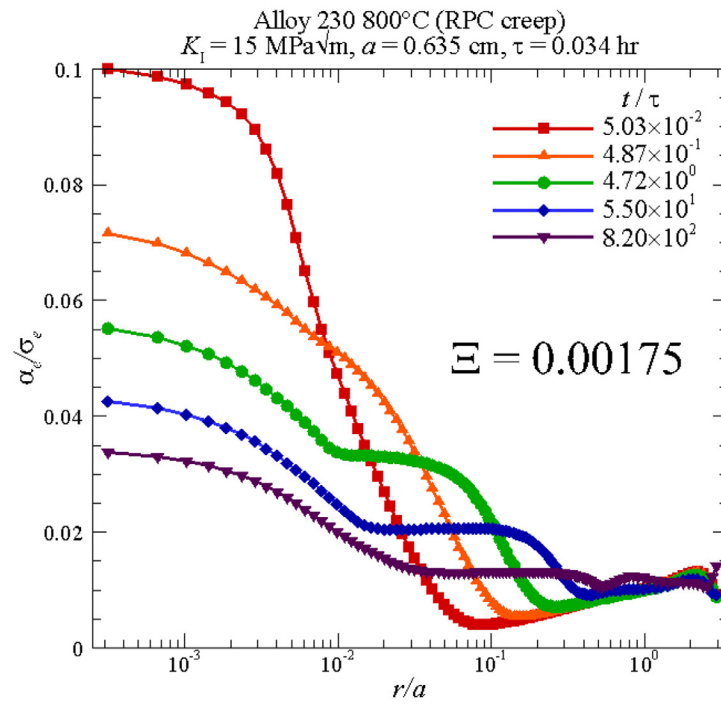
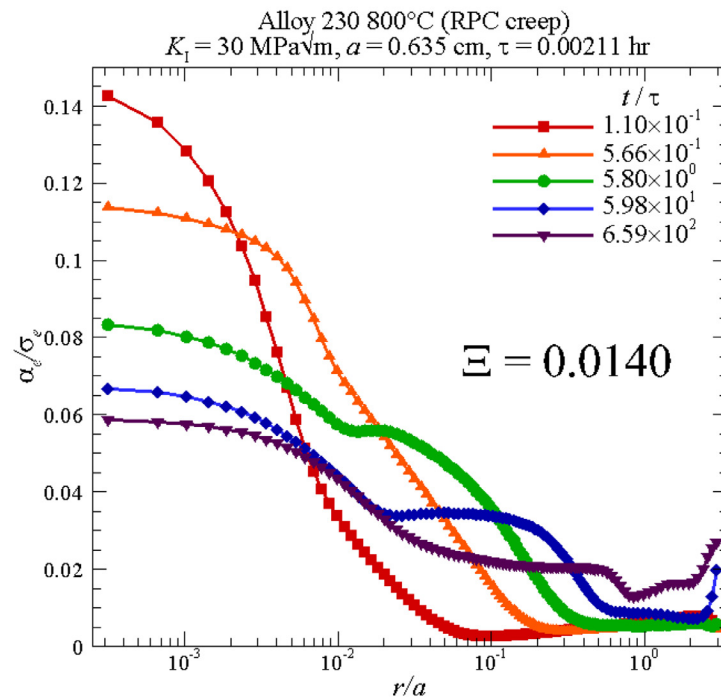


Fig. 7. Numerically simulated opening stress distributions (solid curves) directly ahead of the crack tip (i.e., along the line $\theta = 0$) tip at various times with power-law creep for (a) the Small load, and (b) the Large load. Superimposed are the singular elastic solution (dashed black line) and the corresponding RR solutions (dashed colored lines) at the same times. The material parameters represent Alloy 230 at 800°C. (For interpretation of the references to color in this figure legend, the reader is referred to the web version of this article.)

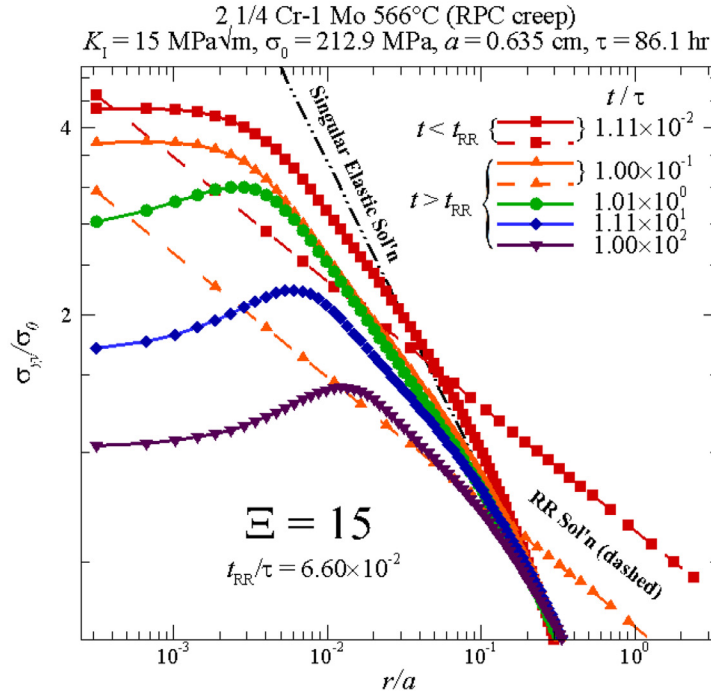


(a)

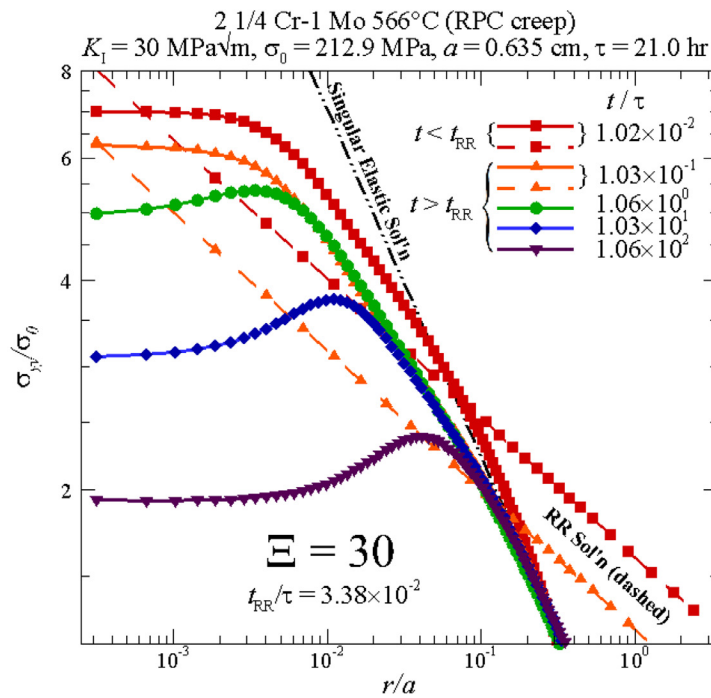


(b)

Fig. 8. Numerically simulated α_e/σ_e distributions directly ahead of the crack tip (i.e., along the line $\theta = 0$) at various times with RPC creep for (a) the Small load, and (b) the Large load. The material parameters represent Alloy 230 at 800°C.

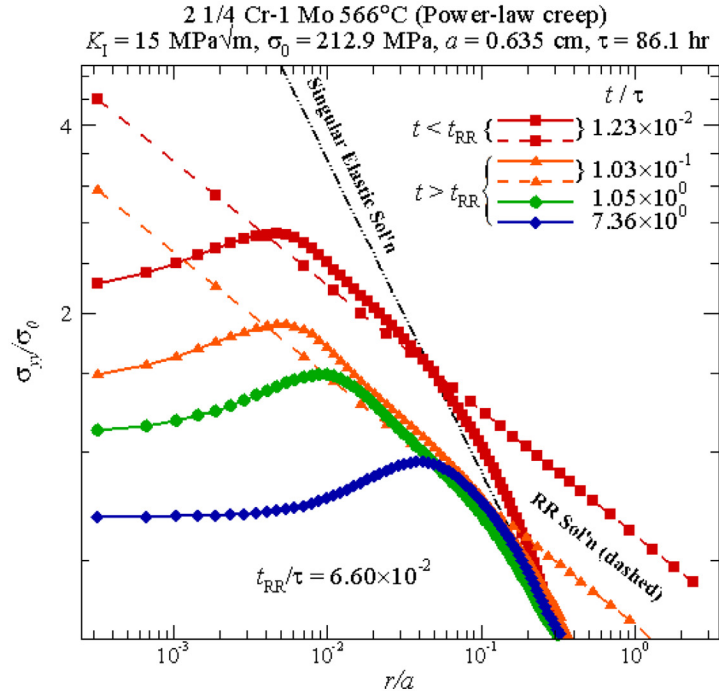


(a)

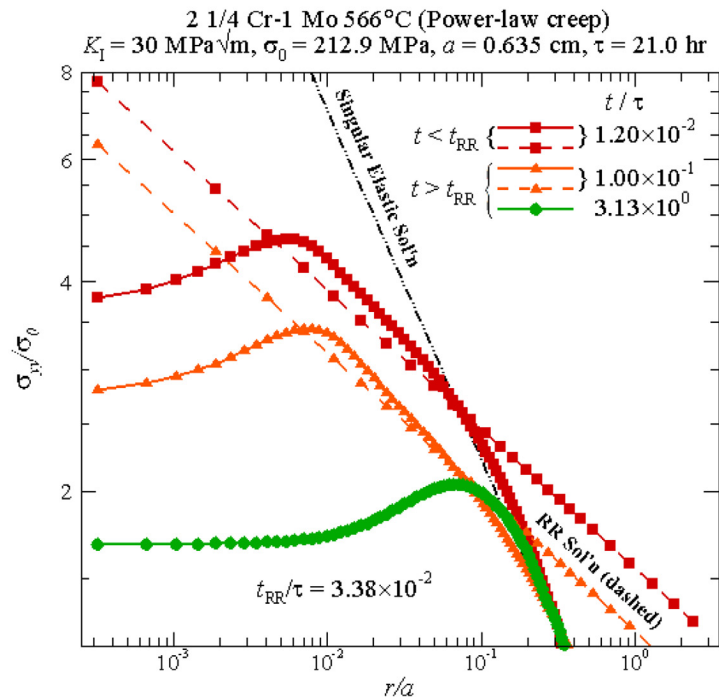


(b)

Fig. 9. Numerically simulated opening stress distributions (solid curves) directly ahead of the crack tip (i.e., along the line $\theta = 0$) at various times with RPC creep for (a) the Small load, and (b) the Large load. Superimposed are the singular elastic solution (dashed black line) and the corresponding RR solutions (dashed colored lines) at the same times. The material parameters represent 2 1/4 Cr-1 Mo Steel at 566°C. (For interpretation of the references to color in this figure legend, the reader is referred to the web version of this article.)



(a)



(b)

Fig. 10. Numerically simulated opening stress distributions (solid curves) directly ahead of the crack tip (i.e., along the line $\theta = 0$) tip at various times with power-law creep for (a) the Small load and (b) the Large load. Superimposed are the singular elastic solution (dashed black line) and the corresponding RR solutions (dashed colored lines) at the same times. The material parameters represent 2 1/4 Cr-1 Mo Steel at 566°C. (For interpretation of the references to color in this figure legend, the reader is referred to the web version of this article.)

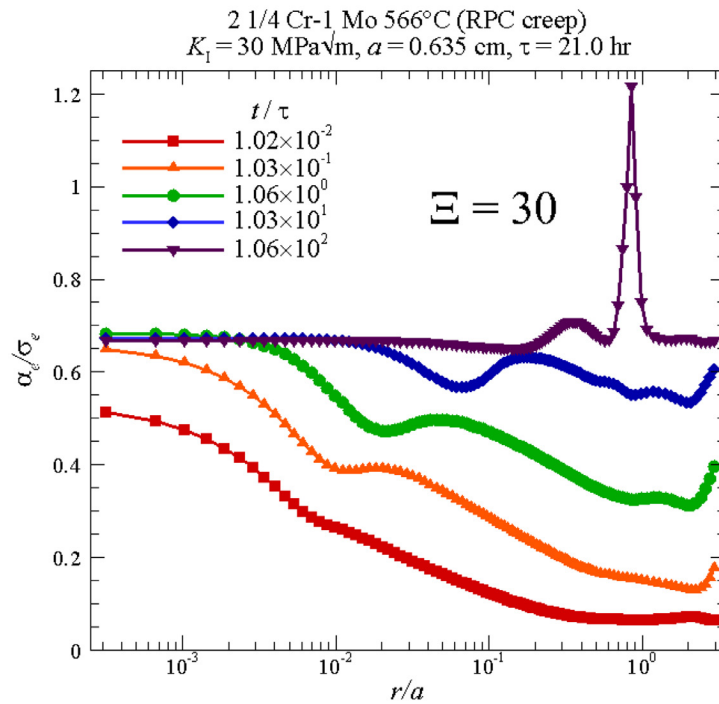
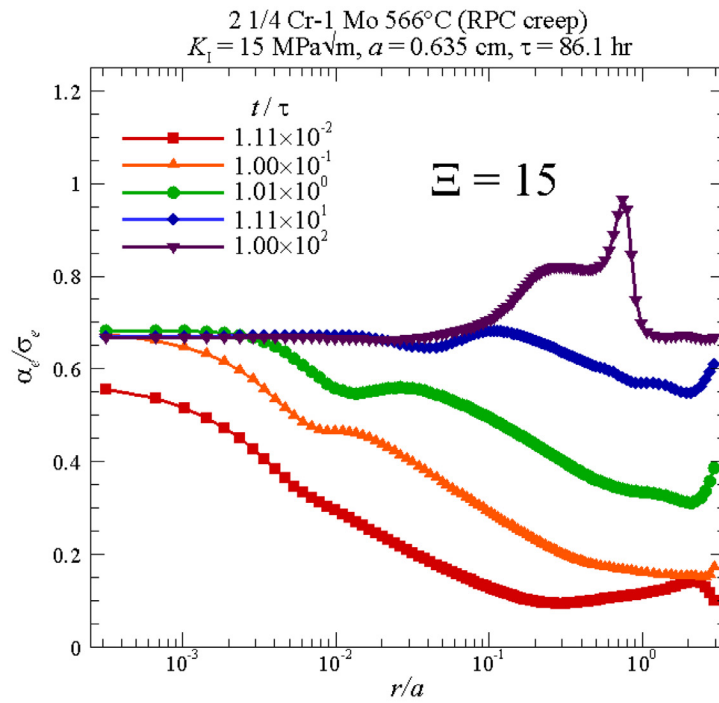


Fig. 11. Numerically simulated α_e/σ_e distributions directly ahead of the crack tip (i.e., along the line $\theta = 0$) at various times with RPC creep for (a) the Small load, and (b) the Large load. The material parameters represent 2 1/4 Cr-1 Mo Steel at 566°C.

set $n = m$). The ratio $\Xi = \tau/t_{RR}$ therefore comes out to about 15 and 30, respectively. Note that, in contrast to the values of Ξ for Alloy 230, which were much less than one, these values are much greater than one. This is consistent with the observation that 2 1/4 Cr-1 Mo Steel exhibits significant primary creep.

Fig. 9 shows the simulated opening stress distributions (σ_{yy}/σ_0 versus r/a) directly ahead of the crack tip ($\theta = 0$) at various times for the two loading levels, using the RPC creep constitutive model calibrated to 2 1/4 Cr-1 Mo Steel at 566°C. Superimposed on each subfigure are the singular elastic solution and the corresponding RR solutions at the same times (again, refer to Appendix A). Here we have estimated the quantities $\tilde{\sigma}_{yy}(0, 4) \approx 2.18$ and $I_4 = 5.25$ from Figures 5.12 and 5.14 of Kanninen (1985). Note that, because the transition from small-scale creep to extensive creep occurs at times much smaller than τ , the RR solution curve for the second time shown is also the RR solution curve for all subsequent times.

Fig. 9 (a) shows the results for the Small load. At the smallest time shown ($t/\tau = 1.11 \times 10^{-2}$), the material exhibits the initial, elastic response under small-scale creep conditions. The transition to extensive creep occurs at $t/\tau = 6.60 \times 10^{-2}$ (between the first and second times shown). Note that the numerically simulated curve at time $t/\tau = 1.00 \times 10^2$ is well approximated by the RR solution within the region defined by $1 \times 10^{-2} < r/a < 1 \times 10^{-1}$. However, none of the curves at earlier times are well approximated by the RR solution. In other words, unlike in Fig. 6, there is no region in which the RR solution gives an accurate approximation to the numerically simulated behavior under small-scale creep conditions, but there is a region in which the RR solution is accurate under extensive creep conditions. This region appears to form at some time at or before $t/\tau = 1.00 \times 10^2$.

Fig. 9 (b) shows the corresponding results for the Large load. The qualitative behavior of this figure is very similar to Fig. 9(a). The major difference is that the region in which the RR solution is accurate for large-scale creep is generally smaller. In fact, this region only extends between $4 \times 10^{-2} < r/a < 1 \times 10^{-1}$ at time $t/\tau = 1.06 \times 10^2$ in Fig. 9(b). Still, it is interesting that the RR solution should be valid at all for the RPC model with these material parameters. We will return to this observation shortly.

Again, it is of interest to see what Fig. 9 would have looked like using power-law creep (with the same creep modulus $A = \dot{\epsilon}_0/\sigma_0^n$ and creep exponent $n = m$). The results for power-law creep are shown in Fig. 10. Again, if the flow stress were negligible compared to the Cauchy stress near the crack tip, we would expect Figs. 9 and 10 to be nearly identical. On the contrary, however, they are quite different. In both Figs. 10(a) and 10(b), there is a region in which the RR solution is accurate *before* the transition from small-scale creep to extensive creep. For example, in Fig. 10(a), this region extends between $5 \times 10^{-3} < r/a < 5 \times 10^{-2}$ at time $t/\tau = 1.23 \times 10^{-2}$. Such a region is not present in Fig. 9. Comparing Figs. 9 and 10, it would appear that primary creep (which is accounted for in Fig. 9 but not in Fig. 10) interferes with the validity of the RR solution under small-scale creep conditions. It seems that the RR solution is not accurate while primary creep prevails, but once the transition to secondary creep has occurred, the RR solution becomes accurate within a finite region ahead of the crack tip.

We conclude this section by verifying that the flow stress is indeed *not* negligible compared to the Cauchy stress for the numerical simulations shown in Fig. 9. Fig. 11 shows the distributions of the ratio α_e/σ_e directly ahead of the crack tip at various times for the two applied loads. In contrast to Fig. 8, in which α_e/σ_e never exceeded about 14%, the vast majority of the curves in Fig. 11 greatly exceed 10%. The local peak that develops just shy of $r/a = 1 \times 10^0$ at time $t/\tau = 1 \times 10^2$ appears to be an artifact, since σ_e is very small there (this is near the point at which σ_{yy} transitions from positive to negative along the uncracked lig-

ament). Disregarding this peak, it appears that as time progresses, α_e/σ_e becomes rather uniform at about 70%, regardless of the applied load. Thus, it cannot be said that the flow stress is negligible compared to the Cauchy stress in these simulations. In light of this observation, it is quite remarkable that the RR solution should be accurate *anywhere* in Fig. 9, and yet that is the case within finite regions for times $t/\tau = 1.00 \times 10^2$ in Fig. 9(a) and $t/\tau = 1.06 \times 10^2$ in Fig. 9(b). One possible explanation is that the RPC model in steady-state creep coincides with, or at least *emulates*, the power-law model.

To summarize, we have shown that, for certain material parameters (representative of Alloy 230 at 800°C), the near crack-tip fields obtained with the RPC creep model are essentially identical to those obtained with classical, power-law creep. Consequently, the RR solution of Riedel and Rice (1980), which was derived for power-law creep, is still accurate—even for RPC creep—within a finite region ahead of the crack tip, under both small-scale creep and extensive creep conditions. For different material parameters (representative of 2 1/4 Cr-1 Mo Steel at 566°C), the RR solution is *not* accurate under small-scale creep conditions. These two distinct behaviors seem to be related to the amount of primary creep exhibited by the specimen, and in particular the dimensionless number $\Xi = \tau/t_{RR}$. When $\Xi \ll 1$ (as it is for the simulations of Alloy 230 at 800°C), it can be said that primary creep is negligible, since the transition to secondary creep occurs long before the transition to extensive creep of the entire specimen. Hence, it makes sense that the near crack-tip results should be almost identical, regardless of whether or not primary creep is accounted for. In contrast, when $\Xi \gg 1$ (as it is for the simulations of 2 1/4 Cr-1 Mo Steel at 566°C), it can be said that primary creep is significant, since the transition to secondary creep occurs long after the transition to extensive creep of the entire specimen. Hence, it makes sense that the results should be different depending on whether or not primary creep is accounted for. In other words, when the specimen exhibits very little primary creep, the RR solution is still valid even with the RPC model, but when the specimen exhibits significant primary creep, the RR solution is not, in general, valid under small-scale creep conditions, prior to the transition to extensive creep. Remarkably, however, it appears that the RR solution is still accurate within a finite region after the transition to extensive creep, even when the specimen exhibits significant primary creep response.

4. Summary and conclusion

In this paper, we have gained new insight into how the stress field ahead of a crack tip in a creeping solid behaves during the transition from primary to secondary creep. We did this by numerically investigating the opening stress distribution predicted by a unified creep-plasticity model due to Robinson et al. (1976). This model accounts for both primary and secondary creep, with a natural transition between the two characterized by the time scale τ , as given by (21). Because large stress concentrations develop near loaded crack tips, and because the RPC model reduces to power-law creep when the flow stress is negligible compared to the Cauchy stress, one might expect the opening stress to be well approximated by the RR solution of Riedel and Rice (1980), which was derived for power-law creep, even when the RPC model is used. However, we have found that this is only the case when the specimen exhibits very little primary creep response.

The extent to which a compact tension specimen exhibits primary creep appears to be well described by a new dimensionless number Ξ , as defined in (29). When $\Xi \ll 1$, the specimen exhibits very little primary creep, since the time spent in the primary creep regime is negligible compared to the time it takes for extensive creep conditions to prevail. Consequently, the flow stress becomes

negligible compared to the Cauchy stress near the crack tip, the near crack-tip fields obtained with the RPC creep model are essentially identical to those obtained with power-law creep, and the RR solution (Riedel and Rice, 1980) is still accurate within a finite region ahead of the crack tip under both small-scale creep and extensive creep conditions. When $\Xi \gg 1$, the specimen exhibits significant primary creep, since extensive creep conditions prevail long before the transition to secondary creep. Consequently, the flow stress is *not* negligible compared to the Cauchy stress near the crack tip, the near crack-tip fields obtained with the RPC creep model are quite different from those obtained with power-law creep, and the RR solution (Riedel and Rice, 1980) is *not* accurate anywhere under small-scale creep conditions. Remarkably, however, there does appear to be a region ahead of the crack tip in which the RR solution is accurate under extensive creep conditions, even when the specimen exhibits significant primary creep. One possible explanation is that the RPC model emulates the power-law model in steady-state creep.

In regard to the relevant loading parameters during a transition from primary to secondary creep, we make the following observations. Regardless of the extent to which the specimen exhibits primary creep, under small-scale creep conditions, there appears to be a region ahead of the crack tip in which the singular elastic solution (Williams, 1957) gives an accurate approximation to the opening stress distribution ahead of the crack tip. Based on this observation, we conclude that the stress intensity factor K_I is still the relevant loading parameter under small-scale creep conditions, in agreement with the conclusion of Ning and Hui (2012). Additionally, as remarkable as it may seem, under extensive creep conditions, there appears to be a region ahead of the crack tip in which the RR solution (Riedel and Rice, 1980) is valid even for RPC creep, regardless of the extent to which the specimen exhibits primary creep. Based on this observation, we conclude that C^* is still the relevant loading parameter under extensive creep conditions. We interpret these conclusions—which are based not on power-law hardening models that treat primary and secondary creep separately, but rather on the integrated RPC creep model Robinson et al. (1976)—as confirming the original conclusions of Riedel (1981), Riedel and Rice (1980), and Ning and Hui (2012). The relevant loading parameter during the transition from small-scale to extensive creep is less clear and requires further analysis.

Declaration of Competing Interest

The authors declare that they have no known competing financial interests or personal relationships that could have appeared to influence the work reported in this paper.

Appendix A. Review of the RR solution

Riedel and Rice (1980) considered a material whose constitutive behavior is governed by a combination of isotropic, linear elasticity and power-law creep (thereby restricting attention to materials that do not exhibit significant primary creep response). The small-strain formulation of the governing equations (local static equilibrium, the material constitutive law, and the strain-displacement relation, respectively) in that case is summarized below:

$$\sigma_{ij,j} = 0, \quad (\text{A.1})$$

$$\dot{\varepsilon}_{ij} = \frac{1}{E} [(1 + \nu)\dot{\sigma}_{ij} - \nu\dot{\sigma}_{kk}\delta_{ij}] + \frac{3}{2}\dot{\varepsilon}_0 \left(\frac{\sigma_e}{\sigma_0}\right)^{n-1} \frac{\sigma'_{ij}}{\sigma_0}, \quad (\text{A.2})$$

$$\dot{\varepsilon}_{ij} = \frac{1}{2}(\dot{u}_{i,j} + \dot{u}_{j,i}), \quad (\text{A.3})$$

where $\dot{\varepsilon}_{ij}$ is the total strain rate tensor, E is Young's modulus, ν is Poisson's ratio, $\dot{\varepsilon}_0$ is a reference strain rate, σ_0 is a reference stress, n is the stress exponent for power-law creep, u_i is the displacement field, and a comma represents the gradient operation, i.e., $(\cdot)_{,j} = \partial(\cdot)/\partial x_j$.

Upon application of an external load, there is an initial elastic response such that the singular elastic solution prevails near the crack tip. Subsequently, the material creeps, and since the stresses are largest in the vicinity of the crack tip, creep accumulates most rapidly there. In this way, a region in which the elastic strain rate is negligible compared to the creep strain rate develops near the crack tip and begins to grow. Within this region (henceforth called the creep zone), the constitutive law (A.2) reduces to

$$\dot{\varepsilon}_{ij} \approx \frac{3}{2}\dot{\varepsilon}_0 \left(\frac{\sigma_e}{\sigma_0}\right)^{n-1} \frac{\sigma'_{ij}}{\sigma_0}. \quad (\text{A.4})$$

Riedel and Rice (1980) noted that the governing equations within the creep zone are the same as those considered by Hutchinson (1968) and Rice and Rosengren (1968), except that the strain field has been replaced by the strain rate field, and the displacement field has been replaced by the velocity field. They concluded that, within the creep zone, the HRR solution holds in rate form. Their solution (known as the RR solution) can be summarized as follows:

$$\sigma_{ij} = \sigma_0 \left[\frac{C(t)}{\dot{\varepsilon}_0 \sigma_0 I_n r} \right]^{\frac{1}{n+1}} \tilde{\sigma}_{ij}(\theta, n), \quad (\text{A.5})$$

$$\dot{\varepsilon}_{ij} = \dot{\varepsilon}_0 \left[\frac{C(t)}{\dot{\varepsilon}_0 \sigma_0 I_n r} \right]^{\frac{n}{n+1}} \tilde{\varepsilon}_{ij}(\theta, n), \quad (\text{A.6})$$

$$\dot{u}_i = \dot{\varepsilon}_0 r \left[\frac{C(t)}{\dot{\varepsilon}_0 \sigma_0 I_n r} \right]^{\frac{n}{n+1}} \tilde{u}_i(\theta, n). \quad (\text{A.7})$$

Here I_n is a known dimensionless function of n ; the quantities with a superscripted tilde are known dimensionless functions of θ and n but not r ;

$$C(t) = \int_{\Gamma} \left(W^* n_x - \frac{\partial \dot{u}_i}{\partial x} \sigma_{ij} n_j \right) ds \quad (\text{A.8})$$

is a path integral Kanninen (1985); the path Γ originates on the lower crack surface, extends counterclockwise around the crack, and ends on the upper crack surface; n_i is the unit outward normal to Γ ; and

$$W^* = \frac{n}{n+1} \dot{\varepsilon}_0 \sigma_0 \left(\frac{\sigma_e}{\sigma_0}\right)^{n+1} \quad (\text{A.9})$$

is a potential function defined such that, within the creep zone,

$$\sigma_{ij} = \frac{\partial W^*}{\partial \dot{\varepsilon}_{ij}}. \quad (\text{A.10})$$

In general, because (A.4) only holds within the creep zone, $C(t)$ is only path independent within the creep zone, and it is understood that the path should be taken within the creep zone.

For small, finite times, when the creep zone is still small compared to the entire specimen (a condition known as “small-scale creep”), Riedel and Rice (1980) argued based on dimensional considerations that the stress tensor must go like $(1/t)^{1/(n+1)}$. Using this result, it is possible to integrate (A.4) directly, and it can be shown that $\varepsilon_{ij} = (n+1)t\dot{\varepsilon}_{ij}$. It follows that $C(t)$ is related to the J-integral (Eshelby, 1956; Rice, 1968) as follows:

$$C(t) = \frac{J}{(n+1)t}. \quad (\text{A.11})$$

They also noted that, for small-scale creep, J is path-independent everywhere in the specimen, and can therefore be related to the stress intensity factor as

$$J = \begin{cases} (1 - \nu^2)K_I^2/E & \text{plane strain} \\ K_I^2/E & \text{plane stress} \end{cases} \quad (\text{A.12})$$

Hence, for small times, the asymptotic crack tip fields are characterized by the stress intensity factor K_I . For large times, when the creep zone has grown to the point of enveloping the entire specimen, $C(t)$ approaches a steady-state value

$$C^* = \lim_{t \rightarrow \infty} C(t), \quad (\text{A.13})$$

which is path-independent everywhere in the specimen. Hence, for large times, the asymptotic fields are characterized by C^* .

Riedel and Rice (1980) defined a useful time scale by equating $C(t)$ in (A.11) to C^* , yielding

$$t_{RR} = \frac{J}{(n+1)C^*}, \quad (\text{A.14})$$

where J is evaluated according to (A.12) depending on the stress state under consideration. As noted in the main text, this time scale characterizes the transition from small-scale creep to extensive creep of the entire specimen.

CRedit authorship contribution statement

John W. Sanders: Conceptualization, Methodology, Software, Validation, Formal analysis, Investigation, Data curation, Writing - original draft, Writing - review & editing, Visualization, Supervision, Project administration. **Mohsen Dadfarnia:** Conceptualization, Methodology, Software, Validation, Formal analysis, Resources, Data curation, Writing - original draft, Writing - review & editing, Supervision, Project administration. **Huseyin Sehitoglu:** Conceptualization, Validation, Resources, Data curation, Writing - original draft, Writing - review & editing, Supervision. **James Stubbins:** Conceptualization, Validation, Resources, Data curation, Writing - original draft, Writing - review & editing, Supervision. **Petros Sofronis:** Conceptualization, Methodology, Software, Validation, Formal analysis, Resources, Data curation, Writing - original draft, Writing - review & editing, Supervision, Project administration.

References

- ABAQUS Unified FEA. Dassault Systemes. <https://www.3ds.com/products-services/simulia/products/abaqus/>.
- ASTM E647-15e1. Standard test method for measurement of fatigue crack growth rates. ASTM International, West Conshohocken, PA, 2015. www.astm.org.
- SA387/A387 Grade 22 Class 2. Brown McFarlane Global Steel Solutions. <http://www.brownmac.com/en/products/chrome-moly-plate/sa387-a387-gr-22>.
- Bammann, D.J., 1984. An internal variable model of viscoplasticity. *Int. J. Eng. Sci.* 22 (8-10), 1041–1053.

- Bassani, J.L., McClintock, F.A., 1981. Creep relaxation of stress around a crack tip. *Int. J. Solids Struct.* 17, 479–492.
- Chaboche, J.L., 1989. Constitutive equations for cyclic plasticity and cyclic viscoplasticity. *Int. J. Plast.* 5, 247–302.
- Chersola, D., Lomonaco, G., Marotta, R., 2015. The VHTR and GFR and their use in innovative symbiotic fuel cycles. *Prog. Nucl. Energy* 83, 443–459.
- Enakoutska, K., Ahad, F.R., Solanki, K.N., Tjipitowidjojo, Y., Bammann, D.J., 2012. Using damage delocalization to model localization phenomena in Bammann-Chiesa-Johnson metals. *J. Eng. Mater. Tech.* 134, 1–9.
- Eshelby, J.D., 1956. The continuum theory of lattice defects. In: *Solid State Physics*. Academic Press, pp. 79–144.
- Horstemeyer, M.F., Bammann, D.J., 2010. Historical review of internal state variable theory for inelasticity. *Int. J. Plast.* 26, 1310–1334.
- Hussein, A.M., El-Awady, J.A., 2016. Quantifying dislocation microstructure evolution and cyclic hardening in fatigued face-centered cubic single crystals. *J. Mech. Phys. Solids* 91, 126–144.
- Haynes 230 alloy. HAYNES International. <http://haynesintl.com/docs/default-source/pdfs/new-alloy-brochures/high-temperature-alloys/230-brochure.pdf>.
- Hutchinson, J.W., 1968. Singular behaviour at the end of a tensile crack in a hardening material. *J. Mech. Phys. Solids* 16 (1), 13–31.
- Kanninen, M.F., 1985. *Advanced Fracture Mechanics*. New York: Oxford University Press.
- Kumar, V., German, M.D., Shih, C.F., 1981. *An Engineering Approach for Elastic-Plastic Fracture Analysis*. General Electric Company, Schenectady, New York.
- Lagneborg, R., 1972. A modified recovery-creep model and its evaluation. *Metal Sci.* 6, 127–133.
- Maldini, M., Angella, G., Lupinc, V., 2010. Analysis of creep curves of haynes 230 superalloy. *Mater. Sci. Forum* 638–642, 2285–2290.
- Ning, J., Hui, C.Y., 2012. Crack tip fields in a viscoplastic solid: monotonic and cyclic loading. *Int. J. Fract.* 175, 39–51.
- Pataky, G.J., Sehitoglu, H., Maier, H.J., 2013. Creep deformation and mechanisms in haynes 230 at 800c and 900c. *J. Nucl. Mater.* 443, 484–490.
- Rice, J.R., 1968. A path independent integral and the approximate analysis of strain concentration by notches and cracks. *J. Appl. Mech.* 35, 379–386.
- Rice, J.R., Rosengren, G.F., 1968. Plane strain deformation near a crack tip in a power-law hardening material. *J. Mech. Phys. Solids* 16 (1), 1–12.
- Riedel, H., 1981. Creep deformation at crack tips in elastic-viscoplastic solids. *J. Mech. Phys. Solids* 29, 35–49.
- Riedel, H., Rice, J.R., 1980. Tensile cracks in creeping solids. In: *Fracture Mechanics: Twelfth Conference*, ASTM STP 700, pp. 112–130.
- Robinson, D.N., 1978. A Unified Creep-Plasticity Model for Structural Metals at High Temperatures. ORNL-Report. Oak Ridge National Laboratory.
- Robinson, D.N., Pugh, C.E., Corum, J.M., 1976. Constitutive equations for describing high-temperature inelastic behavior of structural alloys. In: *Proceedings of Specialist Meeting on High-Temperature Structural Design Technology of LMFBRs*, IAEA Report IWGFR/11.
- Robinson, D.N., Swindeman, R.W., 1982. Unified Creep-Plasticity Constitutive Equations for 2-1/4 Cr-1 Mo Steel at Elevated Temperature. ORNL-Report. Oak Ridge National Laboratory.
- Salehghaffari, S., Rais-Rohani, M., Marin, E.B., Bammann, D.J., 2012. A new approach for determination of material constants of internal state variable based plasticity models and their uncertainty quantification. *Comp. Mater. Sci.* 55, 237–244.
- Sanders, J.W., 2017. *Modeling and Simulation of Creep Rupture in High-Temperature Alloys*. The University of Illinois at Urbana-Champaign Ph.D. thesis.
- Stamm, H., Walz, G., 1993. Analytical investigation of crack tip fields in viscoplastic materials. *Int. J. Fract.* 64, 135–155.
- Tung, H.-M., Mo, K., Stubbins, J.F., 2014. Biaxial thermal creep of inconel 617 and haynes 230 at 850 and 950c. *J. Nucl. Mater.* 447, 28–37.
- Walz, G., Stamm, H., 1993. Numerical investigation of crack tip fields in viscoplastic materials. *Int. J. Fract.* 64, 157–178.
- Williams, M.L., 1957. On the stress distribution at the base of a stationary crack. *J. Appl. Mech.* 24, 109–114.
- Zhou, W., Ren, X., Ren, Y., Yuan, S., Ren, N., Yang, X., Adu-Gyamfi, S., 2017. Initial dislocation density effect on strain hardening in FCC aluminium alloy under laser shock peening. *Phil. Mag.* 97, 917–929.